This is a repository copy of *Combustion inhibition of biomass charcoal using slaked lime and dolime slurries*.

Combustion inhibition of biomass charcoal using slaked lime and dolime slurries

Yufeng Lai [a], Xuanqi Liu [b,*], Callum Fisk [a], Matthew Davies [a], Yunbai Wang [a], Jiansheng Yang [c], Chris du Plessis [d], Liam Cotton [d], Yang Zhang [b], Jon Willmott [a,**]

[a] *Department of Electronic and Electrical Engineering, The University of Sheffield, Portobello Centre, Sheffield, S1 4ET, United Kingdom*
[b] *Department of Mechanical Engineering, The University of Sheffield, Sir Frederick Mappin Building, Sheffield, S1 3JD, United Kingdom*
[c] *The Electrical Engineering College, Guizhou University, Guiyang, China*
[d] *Lhoist Recherche et Développement SA, Rue de l'industrie 31, B-1400, Nivelles, Belgium*

ARTICLE INFO

ABSTRACT

Calcium hydroxide (Ca(OH)$_2$) and magnesium hydroxide (Mg(OH)$_2$) are promising fire suppressors because of their characteristics of nontoxic, cost-effective, and high fire suppression ability. In this work, a comprehensive study of fire inhibition of slaked lime and dolime slurries, containing different ratios of Ca(OH)$_2$ and Mg(OH)$_2$, was implemented for the first time. A synchronised imaging system was developed for the visualisation of the droplet evolution temporally. The chemical components were analysed by X-ray diffraction and thermogravimetric analysis. A single droplet test and a variable volume test were performed to measure the charcoal surface temperature under different conditions. The results demonstrated that the Ca(OH)$_2$ slurry better inhibits combustion in comparison to water, which could significantly decrease the risk of fuel re-ignition. The main mechanism was found as the effective inhibition of the exchange of the oxygen and fuel by the thermally stable residues. Additionally, either adding the mixture of Mg(OH)$_2$ or increasing the solid content of the Ca(OH)$_2$ could further improve their effectiveness. Three stages of the fire suppression were identified in this work and a conceptual model was built accordingly to demonstrate the fire inhibition mechanisms. The results from this work could provide important guidance for the research into alternative methods of fire extinguishment.

1. Introduction

Natural fuel resources, such as wood, charcoal and coal, have an important role in the development of industry because they serve as the main source of energy for the generation of heat and power [1]. However, the natural fuel resources pose a significant fire risk in storage [2] because their flammability could cause spontaneous combustion [3], which can lead dust explosion caused by the generated combustible gases if the fire cannot be controlled in time [4]. Therefore, the development of a high-efficiency combustion inhibition agent for the natural fuel is desired and critical for safety and effective utilisation of natural fuels [5].

There are two effective methods for inhibiting the combustion of natural fuels: 1) lowering the fuel temperature to keep it below the ignition point, and 2) preventing the interaction between fuels and oxygen to halt combustion reactions directly [6]. Water has been used as

the primary fire suppression agent throughout human history because it is non-toxic, abundant, and has a high cooling effect [5,7].

Nonetheless, water is inadequate for fire suppression in high temperature applications because its rapid evaporation fails to prevent fuel re-ignition [8]. Aqueous film-forming foams (AFFF) have been considered as an alternative fire suppressant that could prevent fuel re-ignition effectively [9,10]. However, most AFFFs cause environmental contamination during use. Likewise, film-forming fluoroprotein foam (FFFP) exhibits good performance for fire suppression [11]. However, they pose a great threat to the environment and public health [12]. Liquid nitrogen (LN$_2$) is another promising fire suppression agent due to its nontoxic nature, high volatility, and low temperature. It has been widely used in biological, electronic, and aerospace-based applications [8]. However, LN$_2$ cannot extinguish fires and prevent further combustion reactions from a distance, due to its high volatility.

Additionally, researchers have explored of the use of dry powders as

alternative fire suppression agents [13]. Metallic-based additives [14], such as zinc borate [15], expandable graphite [16], magnesium hydroxide [17] and zinc hydroxy stannate [18] have been proven to be effective agents because they form a thermally stable layer which hinders the combustion process and heat transfer. However, the suppression effectiveness of these metallic-based agents is poor at high-temperature [19]. This is because the lack of cooling effects of those dry powders. Furthermore, the cost and the difficulty in preparation make these additives challenging for use in practice.

Calcium-based materials are promising as an alternative fire suppression agent because of their high suppression ability and they are renewable, nontoxic, and available at low-cost. Researchers reported the high suppression capability of calcium carbonate ($CaCO_3$) [20,21]. Koshiba et al. investigated the flame inhibition ability using various calcium compound suppressants [22]. Hamdani-Devarennes et al. investigated the fire reaction using calcium and aluminium-based additives. They found that the calcium-based fillers show good fire suppression which is attributed to their thermal stability [23]. Apart from the thermal stability of the calcium residuals, the endothermic dehydration of calcium hydroxide ($Ca(OH)_2$) could increase the fire suppression ability and prevent the occurrence of re-ignition [24]. Laoutid et al. investigated the fire-retardant behaviour of calcium-based hydrated minerals and used lime (calcium-based hydrated minerals) and dolime (both magnesium and calcium hydroxide) as fire resistant additives to broaden the effective temperature range of fire suppressor [19, 25]. Huang et al. combined $Ca(OH)_2$ with polymer-based composite to improve the inhibition performance on coal combustion [26].

In addition to the fire suppression ability, calcium-based materials were developed as adsorbents for capturing CO_2 generated from charcoal or other biomass fuel [27,28]. This property makes calcium-based materials ideal to serve as the fire inhibitor of the natural fuels since the generated CO_2 would accelerate the form of thermal-stable $CaCO_3$ layer [29].

Calcium-based hydrated minerals have been investigated for fire suppression in the literature, though only as fillers or additives in the solid-phase. The liquid-phase agent plays a crucial role in extinguishing a large-scale fire, not provided for by solid powder due to the nature of diffusivity and volatility. In addition, the liquid-based agent can provide effective cooling effect on the burning fuels because the endothermic evaporation of water. It is of great significance to investigate the fire suppression ability of calcium-based hydrated minerals as a slurry. Small-scale experiments are necessary for revealing the fundamental characteristics of liquid since they are practical to analyse quantitatively [30]. Single droplet tests are widely used for investigating the mechanisms of a specific liquid because they can represent behaviours in large-scale scenarios [31].

According to the literature, several topics have yet to be studied: 1). Calcium-based hydrated minerals (lime slurry) or calcium & magnesium-based hydrated minerals (dolime slurry) could provide promising performance in fire suppression based on the properties that have been discussed already. However, at the time of writing there are no publications systematically investigating the fire inhibition capabilities of those slurries, particularly for natural fuel resources. 2). A single droplet can represent the fundamental mechanisms of large-scale liquid, and so it is of great importance that the different calcium/magnesium-based droplets impacting on a burning surface are visualised. 3). In order to apply the new fire inhibitor, comprehensive research which includes the ability of spreading and fire inhibition is necessary. A conceptual model indicating the fire inhibition mechanisms at different stages is required as the framework for the subsequent design and applications in practice.

Imaging-based analytical metrology has advantages over traditional invasive sensors, such as thermocouples, for our studies of fire suppression. This is due to the rapid evolution of the characteristics of the liquid. We utilise high-speed Schlieren imaging for efficient visualisation of heat flow fields and potential phase transfers [32,33].

Non-contact thermal imaging is used for instantaneous temperature profiling without disturbing the experimental system [34,35].

This work aims to reveal the effectiveness of combustion inhibition of calcium & magnesium based hydrated slurries. A charcoal cube was used as the solid-phase fuel base, due to it is representative of biomass fuels and it has the similar combustion reactions to coals. A comprehensive study was achieved using synchronised imaging and analytical metrology. The high-speed colour imaging system could visualise the process of a droplet impacting with the unburnt/burning surface of the fuel. The spread factor was obtained during post-processing. The high-speed Schlieren imaging system was able to track diminutive density changes, which represent the phase change of water that cannot be captured in the visible spectrum. Two thermal cameras were used for monitoring the charcoal surface temperature temporally. The cooled area and the inhibition of re-ignition could be quantitatively studied with post-processing.

The characteristics of the interactions of slaked lime and dolime slurries with fire are presented here in literature for the first time. The insights gained in this work may provide an important framework for future studies of alternative fire suppression agents for natural fuels. The study from present work could be used in the fields relate to fire inhibition of natural fuels, such as the coal industry, energy storage and generation sectors, and fire inhibition of wooden structures.

2. Methodology

2.1. Experimental arrangement

The imaging system used in the work is illustrated in Fig. 1 (a). Four cameras were synchronised by a trigger system. They are: 1. A high-speed colour camera mounted with a micro-focus lens targeted the top surface of the sample and was able to capture the detailed process of the wetting, spreading and evaporation. 2. A monochromatic high-speed camera was used to provide a Z-type Schlieren imaging system. This was sensitive enough to visualise the hot flow around the burning samples and any phase change during and after the impact of the liquid droplets. 3. A long-wavelength infrared camera (LWIR) which has the capability to detect the object's temperature at room temperature was used for measuring the surface temperature of the samples during the impact. 4. A short-wavelength infrared InGaAs camera (SWIR) was used for monitoring the temperature change of the cooled area due to its high-resolution and relative fast framerate. A narrow band-pass filter was used to restrict its spectral sensitivity to 1490–1500 nm.

The test zone is shown in Fig. 1 (b). Charcoal cubes were selected as the test samples in the work because of their homogeneousness. The charcoal we selected was made from coconut shells which is common in domestic and industrial applications. In addition, charcoal is a fuel that includes solid-phase combustion (pure carbon) and gas-phase flaming (14% volatiles [36]), which is ideal to represent the properties of biomass fuels. Charcoal is also a common material which would exist in many types of fire [37]. The dimensions of the cube were 25 mm × 25 mm x 25 mm, and the emissivity was assumed as 0.78 [38,39].

A premixed methane-air jet flame with flowrates of 0.7 L/min and 1.8 L/min respectively was used to ignite the samples in order to keep a stable impinging flame and limit soot influence, ensuring the experimental results were consistent. A sample holder was designed for the purpose of minimising the interference of flow field around the sample. The burner nozzle was 5 mm in diameter and the distance between the nozzle and the bottom surface of the sample was kept as 78.54 mm. Each sample was pilot ignited for 30 s then self-sustained ignition for another 30 s before the liquids impacted for the uniformity of the inner heat distributions.

2.2. Preparation of liquids

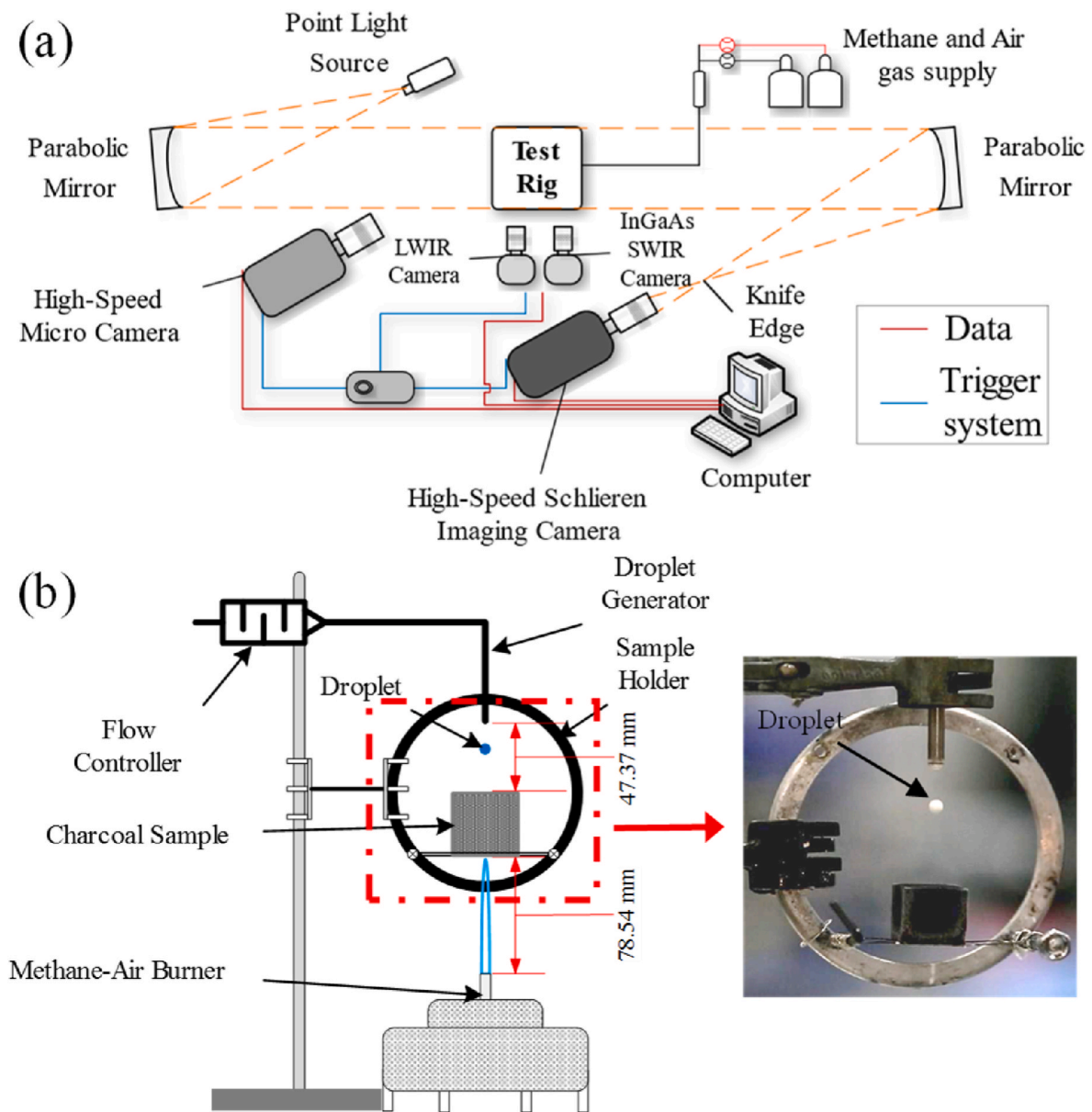Four different types of liquids were used in this study: distilled water,

Fig. 1. Demonstration of the experimental setup: (a) imaging systems and the gas supply and (b) the test rig.

SLS20, SDS20, and SLS45. The detailed descriptions of each slurry are presented in Table .1.

The liquid generator designed for the work was fixed above the

Table 1
The solid content of each slurry.

Label	Control	SLS20	SDS20	SLS45
Product description	Distilled water	Slaked lime slurry	Slaked dolime slurry	High solids content slaked lime slurry
Dominate chemical component	H_2O	$Ca(OH)_2$ H_2O	$Ca(OH)_2$ Mg $(OH)_2$ H_2O	$Ca(OH)_2$ H_2O
Solid content (wt %)	–	19.93%	20.93%	44.38%
Ca: Mg mass ratio	–	99:1	59:41	99:1
Particle size range (μm)	–	2–21	1–36	1–10
Droplet diameter (mm)	5.72 ± 0.29	5.61 ± 0.24	5.57 ± 0.33	5.24 ± 0.12

sample surface at a distance of 47.37 mm. This liquid generator contained a flow controller which controlled the volume of output fluids, a tube for conveying the liquids and a nozzle with 3.2 mm inner diameter to control the droplet size. All the slurries were kept mixing in an ultrasonic mixer to ensure the uniformity. The droplet was formed as the liquid was ejected at the tip of the nozzle. The droplet diameters were measured by the high-speed camera imaging by comparison with a pre-calibrated pixel field-of-view (FOV), as shown in Table 1. Due to the difference in surface tension and mass of the different liquid droplets, the diameter was slightly different between the samples. A series of dimensionless analytical approaches were utilised in the work to cancel the influence of the droplet diameter difference, which will be discussed in the image processing section.

Various volumes of liquids were used to investigate the effectiveness of temperature suppression. One single droplet was used to visualise the phenomena of spreading and evaporation for each type of liquid and to measure the temperature change after impacting as a fundamental element. Then, 0.5 ml, 1 ml, 2 ml, 3 ml, and 5 ml of each liquid was applied to reveal the suppression utility and validate the findings

obtained from the single droplet experiments. Each experiment was repeated between three and five times, to ensure repeatability.

2.3. Image processing

Image processing was used to investigate the performance of liquids with various chemical components. The wetting, or spreading rate is an essential characteristic for fire suppression [40]. The spreading rate is strongly related to the surface tension of the liquids [41], therefore, it is of great interest to characterise the different spreading capabilities temporally for each liquid sample.

Monitoring the wetted area precisely is a challenge because of the transparency of water droplets and the irregular pattern and the lack of contrast between the wet and dry areas. A series of image processing methodologies were applied for obtaining the instantaneous wetted area profile, including noise cancelling, selective enhancement, image segmentation, binarisation, edge detection and tomographic reconstruction. Fig. 2 shows the raw colour images and the detected wetted area at typical frames, it can be seen that the output results show a good agreement with the original images.

The wetted area was nondimensionalised to remove the difference of the droplet dimension and provides more comparable insights into the ability each liquid to wet the surface. The pixel field-of-view (FOV) of the camera was calibrated with a reference object; the spread factor could then be calculated according to Equation (1):

$$D/D_0 = \frac{2 * \sqrt{A * L_{px}^2 / \pi}}{D_0},$$ (1)

Where D/D_0 represents the spread factor of each droplet, D_0 is the initial droplet diameter (which was measured by the high-speed imaging), A is the number of pixels of the wetted area which was detected by the algorithm and L_{px} is the length the occupied the FOV of each pixel that was calibrated before the experiment.

LWIR thermal images were utilised for monitoring the top surface temperature of the charcoal samples temporally and were used to investigate the temperature suppression ability of different liquid droplets. Example thermal images are shown in Fig. 3. The region of interest (ROI) was determined according to the maximum wetted area D_{max} which was calculated by equation (2). The temperature was averaged across the ROI in order to eliminate the influence of the different wetting abilities and provide a more accurate dimensionless result (see Fig. 4).

$$D_{max} = 2 * \sqrt{A_{max} * L_{px}^2 / \pi},$$ (2)

where D_{max} represents the maximum wetted area which occurred at the initial stage of the process, A_{max} stands for the detected number of pixels when the wetted area was maximum.

The InGaAs SWIR camera was used for monitoring the cooled area evolution on the top surface of the samples. Comparing with the average temperature, the size of the cooled area provided another metric for the ability of the liquid-under-test to supress combustion. This was calculated by counting the area under a fixed threshold. The threshold was set as 300 °C according to its predicted internal temperature distributions [42] and the pyrolysis temperature of biomass [43,44]. The results were normalised for intuitive comparison between the different droplets, shown in Eq. (3).

$$D/D_{max} = \frac{2 * \sqrt{A * L_{px}^2 / \pi}}{2 * \sqrt{A_{max} * L_{px}^2 / \pi}} = \sqrt{\frac{A}{A_{max}}}.$$ (3)

2.4. Temperature measurement

Two thermal cameras, LWIR (PyrOptik, model LW640) and InGaAs SWIR (PyrOptik, model NIRIN640), were used in the work for measuring the charcoal top surface temperature. The LWIR camera was sensitive to the wavelength range from 7.5 μm – 13.5 μm which enabled it to detect the surface temperature when the droplet impacted. The camera has 640 × 512 pixels with a fixed framerate of 9 Hz. This was calibrated from 50 °C to 650 °C using an approximate blackbody furnace (emissivity ~ 0.99) at increments of 50 °C. 100 images were captured and averaged to obtain the digital value (DL) output from the temperature at each temperature. Fig. 5 (a) shows the calibration curve and measured uncertainty (red line) of LWIR camera. The fitted curve showed a good agreement with the blackbody temperature (R^2 = 0.9999). It is found that the maximum residual was less than 10 °C which provides adequate performance for the purposes of this research.

The InGaAs SWIR camera has a 2048 × 2048 pixel resolution with a framerate of 60 Hz. This allowed more detailed imaging, than LWIR measurements, and enabled monitoring of the temperature of the cooled area temporally. The spectral sensitivity was restricted in the range of 1490 nm – 1500 nm to obtain an accurate temperature reading from 250 °C to 700 °C. The calibration was based on Planck's Law [45], 100 images were captured and averaged with a blackbody furnace (emissivity ~ 0.99) between 250 °C and 700 °C, at increments of 50 °C. The offset from zero digital-logic-levels, under unilluminated conditions,
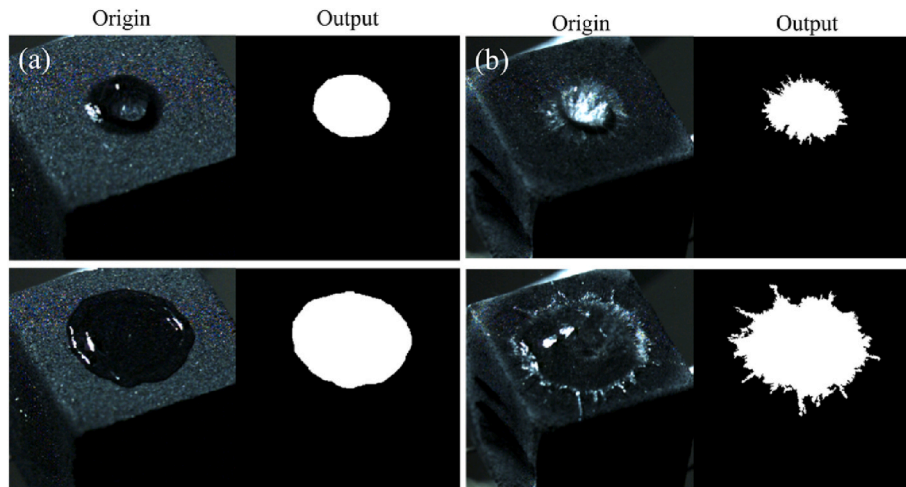

Fig. 2. Illustration of the wetted area: (a) impacted on an unburnt surface (b) on a burning surface.
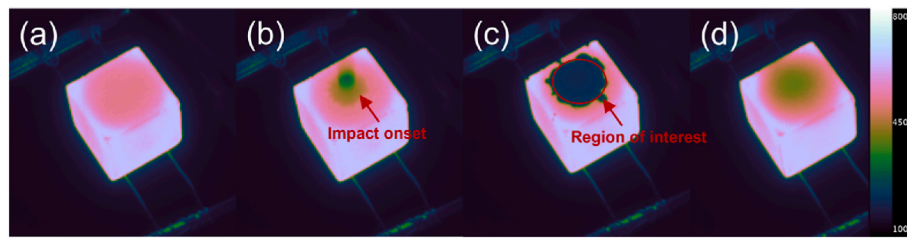
Fig. 3. Example LWIR thermal images indicating the region of interest and the different stages of droplet impact: (a) The moment before the droplet impacted, (b) the droplet impact onset, (c) maximum wetting and (d) temperature increase after evaporation. Red circle indicates the region of interest using for the quantitative measurements. (For interpretation of the references to colour in this figure legend, the reader is referred to the Web version of this article.)
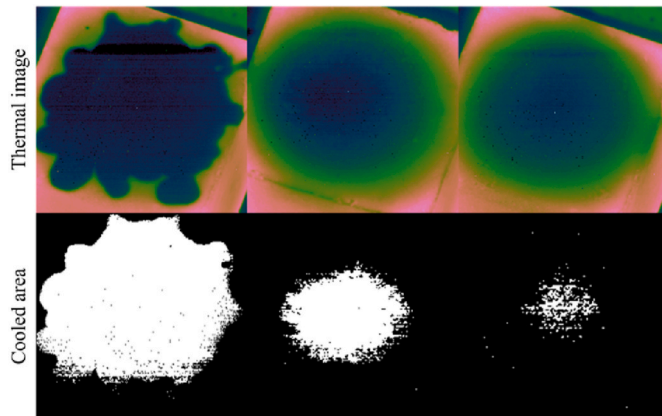

Fig. 4. Illustration of the InGaAs SWIR thermal images and the processed cooled area ($T \leq 300°C$) at different stages.

was determined by averaging 100 images with the lens covered. The calibrated temperature curve is shown in Fig. 5 (b). It was found that the uncertainty of InGaAs camera was less than 5 °C across the specified temperature range of 300 °C–700 °C.

2.5. Component analysis

2.5.1. Thermogravimetric analysis (TGA)

TGA experiments were conducted to investigate the decomposition reactions of the slaked lime and dolime samples under the non-combustion condition and provide insights on the temperatures of chemical reactions occurring. Samples were dried at 150 °C for 10 min and a 3 g dried powder sample of each was subjected to loss-on-ignition (LoI) thermogravimetric measurement using a Las Navas Instruments

Automatic Multiple Sample Thermogravimetric Analyzer TGA-2000. The heating rate was set to 5 °C/min.

2.5.2. X-ray diffraction (XRD)

Calcium-based and magnesium-based hydrated minerals can decompose into different components under high temperature [46]. Therefore, component analysis was necessary in order to investigate the possible chemical changes during the process. Three different groups of samples were prepared: 1. The original slurry. 2. The remaining layer after 30 s of the droplet impact. 3. The remaining layer after 5 min of the droplet impact. The test groups are shown in Table 2. Sample 2 was determined to represent the chemical change during the temperature increase (obtained from our temperature measurements), after the initial cooling. For sample 3, it was determined that most of the hydrated minerals had decomposed completely.

The component analysis was carried out using X-ray diffraction analysis (XRD). The diffraction patterns were collected on the PANalytical Aeris with Bragg-Brentano reflection geometry. A 0.02 mm Ni Kβ filter was applied, incident and diffracted slits were 0.04 Rad Soller with ¼° divergence. An air scattering beam knife was employed, and the sample sinner was 0.5 Hz. The 2-theta range was from 10 to 100° with a 0.02° step size. The sample holder used was 27 mm in diameter and 3 mm in depth. The original slurries (test group 1) were carefully dried at a lower temperature than their decomposing temperature and ground into a fine powder. CO_2 was isolated in this process preventing any possible carbonation. Regarding test groups 2 and 3, the remaining layers were scratched from the charcoal sample carefully and stored in a vacuum to

Table 2
XRD groups of samples.

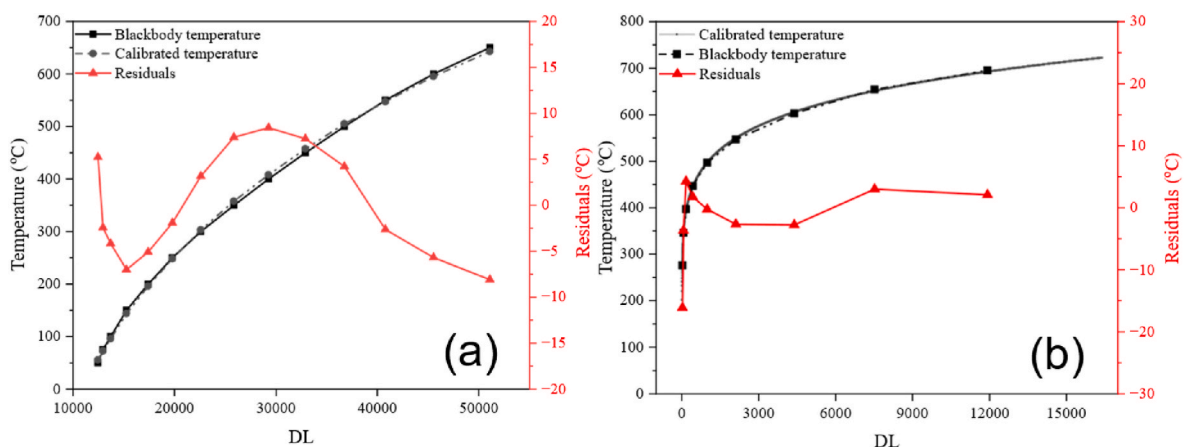| Test groups	1	2	3
Heating duration	None	30 s	5 min

Fig. 5. Radiance calibration curve and uncertainty of measured temperature. (a) LWIR camera and (b) InGaAs SWIR camera.

avoid contamination from moisture and carbon dioxide.

3. Results

The ability of combustion inhibition of different types of liquids was investigated from four aspects: spreading (or fluidity) properties were presented in Section 3.1; The visualisation of gas-phase change was shown in Section 3.2; The evolutions of surface temperature and the cooled area size were presented in Section 3.3; and the chemical component analysis was shown in Section 3.4. With the comprehensive investigation, the combustion inhibition mechanisms can be revealed and a conception model was built in the Discussion section.

3.1. Spreading capability

3.1.1. Impacted on an unburnt surface

The capability of each liquid to spread, covering the surface of the fuel is one of the most important characteristics of the liquid droplet and determines its wetting ability. It is also a crucial factor of a liquid-based fire suppressor in order to utilise it for suitable conditions. The spreading factor ($D_{/D_0}$) can provide a comparison of the ability of spreading between liquids.

Fig. 6 shows the single droplet spreading and wetting process on unburnt charcoal. It was observed that the droplets started to spread within the first 2 ms and completed this process approximately 30 ms after impact. The water droplet had the largest wetted region (shown as the red circles) which indicated it has the widest spreading ability on an unburnt surface. The wetting process was observed at the same time as the spreading and it was noted that this lasted longer. It took 150 ms for the water droplet and increased proportionally to the solid content of the liquid. There were layers of residue on the surface of the SLS20/SDS20/SLS45 droplets after the wetting process had completed. The polyporous layers (SLS20 and SDS20) became denser and thicker with increasing solid content within the droplet.

The spreading factor droplets varied with different experimental arrangements. The spreading factor of water has previously been observed in the typical range of 1.25–4.5 when the droplet impacts on a dry solid surface [47]. In this work, the spreading factor of water was approximately 3.25 (shown in Fig. 7), which was 41% greater than the SLS20 droplet, 23% greater than the SDS20 droplet, and 86% greater than the SLS45 droplet. The decreased spreading factor was attributed to the increased surface tension of the $Ca(OH)_2/Mg(OH)_2$ slurry. These results provide a general indication of the wetting and absorption performance of the different fluids, although the spreading factor could differ under various scenarios or when impacting on a hot surface. In detail, a greater spread factor suggests that the liquids can evaporate
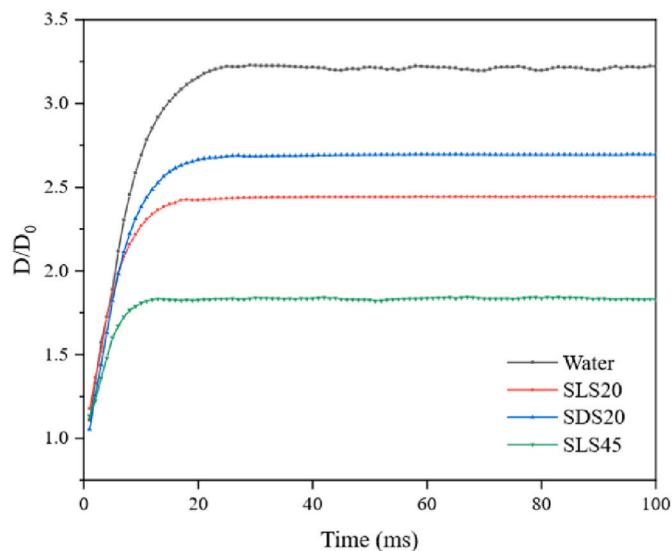

Fig. 7. The spreading factor of different component droplet impacts on an unburnt surface.
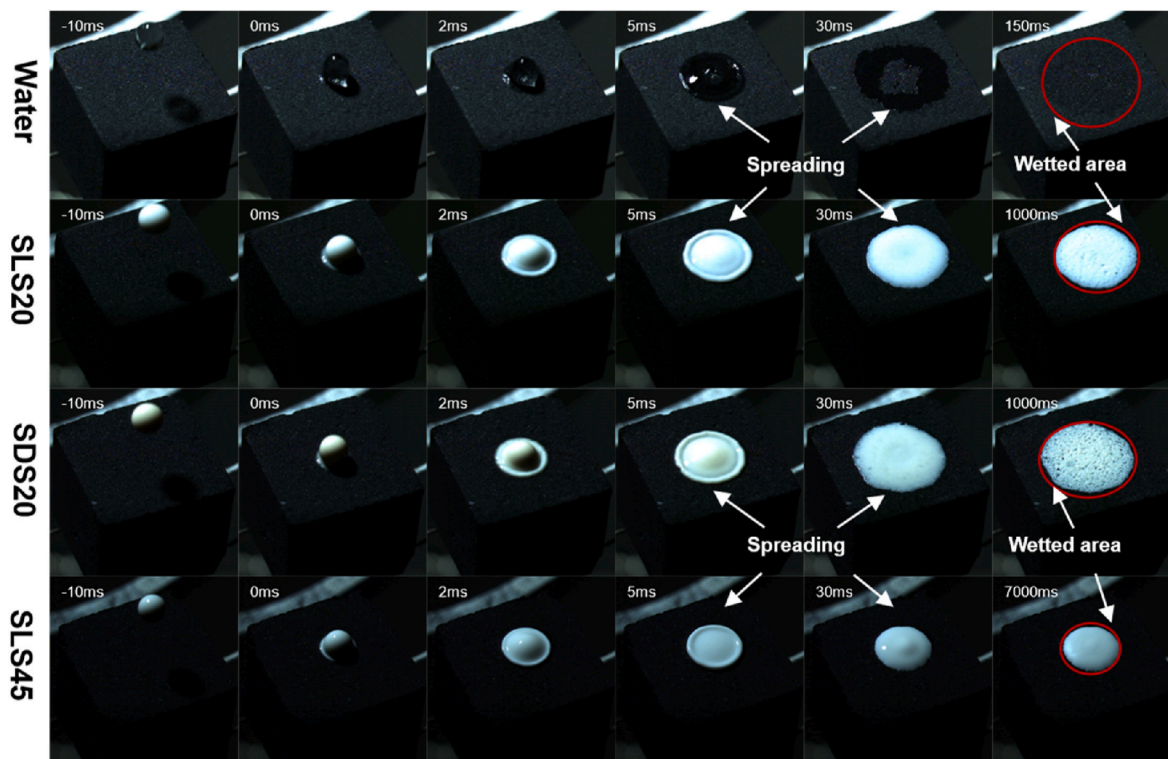

Fig. 6. The time evolution of a droplet impact on the unburnt charcoal surface.

effectively, while the smaller spread factor indicates that the liquids have a better adhesion providing a better local performance.

3.1.2. Impacted on a burning surface

The droplets impacting with a burning surface present significantly different behaviours than those with a cold surface. Albadi and Zhang reported that when a water droplet impacted with burning/cold wooden samples, the spreading factor was significantly larger when the droplet impacted with the burning surface compared to the cold sample [31]. Fig. 8 shows the time evolution of droplets impacting with a burning charcoal surface. The larger spreading factors of the droplets were found for the burning surface, and the droplets spread to their maximum area faster on the burning surface than the cold sample. This is because of the shortened kinematic phase when impacting with a hot surface because additional energy is available [47].

The kinematic phase of droplet impact is the initial stage when the droplet first contacts the surface, with behaviour driven by properties like velocity, size, and impact angle. Following this, the droplet enters the spread phase, where its momentum causes it to spread radially across the surface, influenced by factors like droplet and surface properties, and surrounding air conditions. The temperature of the surface can alter these phases, with hot surfaces potentially causing rapid evaporation, leading to effects like the Leidenfrost phenomenon, which can shorten the kinematic phase and affect the spread phase.

The droplets boiled intensely when the spread phase of the droplet ended (shown as 20 ms in Fig. 8). Fig. 9 shows the maximum spread factors averaged from the multiple tests and their standard deviation. It was found the spread factors decreased proportionally to the solid content of the liquid. Additionally, the SLS45 had the lowest standard deviation indicating the smallest fluidity among the liquids.

The water droplet receded after it reached the maximum spreading area, this was also previously observed when the water droplet impacted with burning wood [31]. Contrarily, the SLS20 and SDS20 droplets tended to evaporate locally as sub-droplets, which was observed in this work for the first time. The images suggested that the polyporous
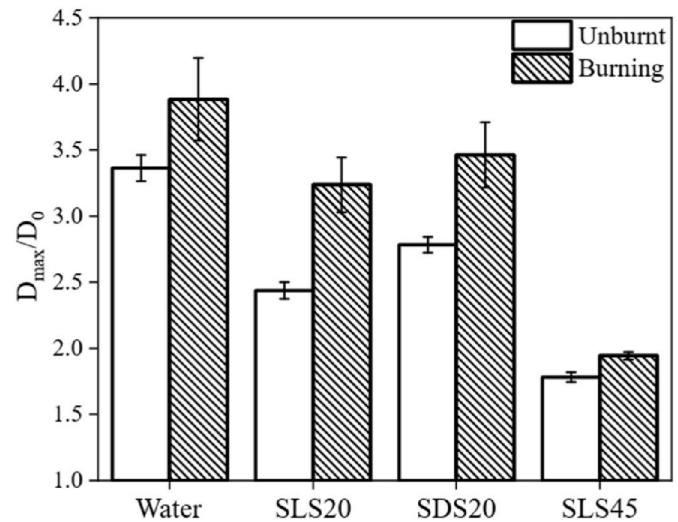

Fig. 9. The comparison between the maximum spread factor on unburnt and burning surfaces with the standard deviation of multiple tests.

structure of the solid layer of SLS20 and SDS20 droplets prevented the clustering phenomenon. In addition, the change in surface tension also contributed to this phenomenon. The content of inorganic compounds in the SLS20 and SDS20 liquids increased the surface tension which helped the sub-droplets evaporate locally. The clustered liquid layer (which presented as bubbling) behaved as a sealant that prevented the subsequent contact between the charcoal surface and the surrounding air, which inhibited the combustion reactions. The main combustion process in charcoal combustion is when solid carbon reacts with the oxygen supply in the air through the polyporous structure [48] this process is similar to the primary combustion reaction of coal, shown as Eq. (4). Additionally, it is also reported in the literature that commercial charcoal has about 14% volatiles generated from the pyrolysis which act as a
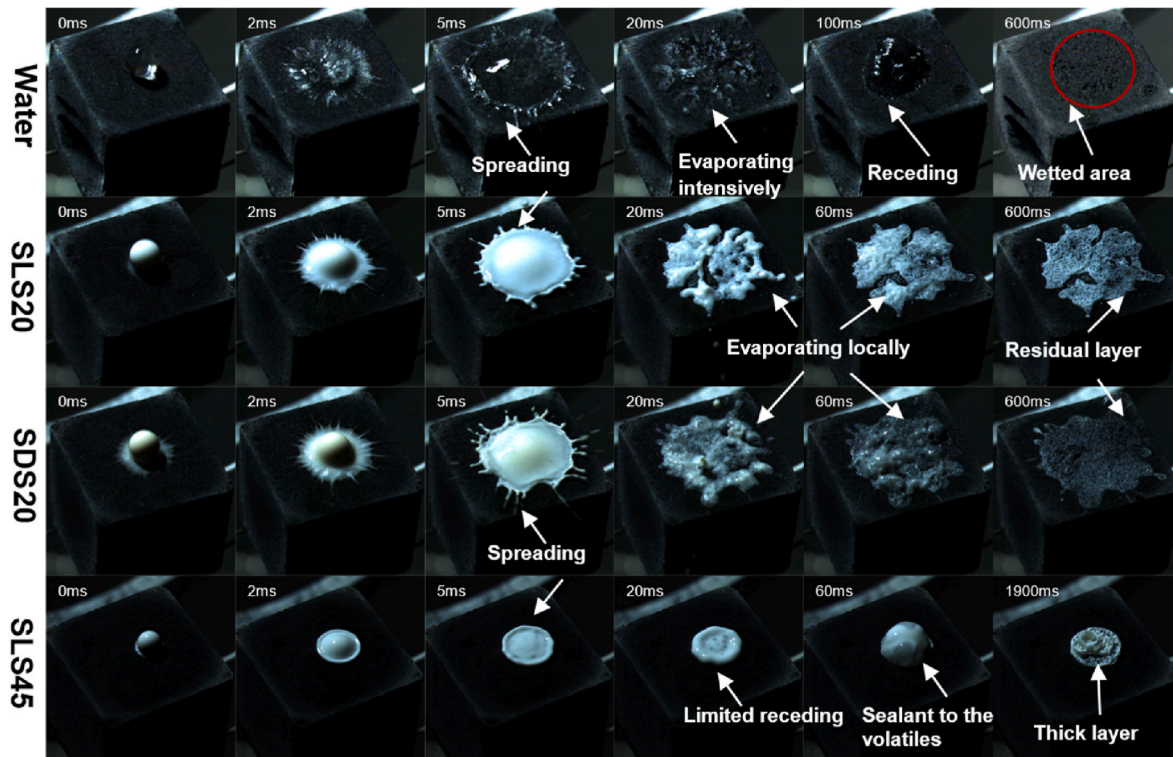

Fig. 8. The process of different types of droplets impacting with the burning surface.

gas-phase fuel similar to other biomass fuels [36,49]. Equation (5) demonstrates the gas-phase combustion of general biomass fuels [50].

$$C + xO_2 \rightarrow aCO + bCO_2 \qquad (4)$$

$$C_aH_bO_c + xO_2 \rightarrow yCO_2 + zH_2O \qquad (5)$$

The liquid sealant not only prevented air entrainment for the solid-phase combustion but also blocked the combustible gases escaping from the solid fuel [51], which acted as an additional mechanism for fire suppression. Local evaporation in SLS20 and SDS20 droplets increased the effective surface area. High concentrations of calcium hydroxide (44.38%) and thus lower water content in SLS45 droplets led to more significant local evaporation. It was found that the SLS45 droplet did not break into sub-droplets in 20 ms, and the receding was limited. A considerable number of combustible volatiles were trapped by the mixed layer, shown as SLS45 60 ms in Fig. 8. The blocking of the exchange of fuel and oxidiser is considered as the most effective approach to prevent combustion reaction [34].

Similarly, the droplets of SLS20/SDS20/SLS45 also left a thick layer after all the moisture had been removed, in addition to the remaining solid residue on the cold surface. The thick layer left by the SLS45 droplet presented as a polyporous structure which differed from when it impacted with a cold surface. This provided further evidence that the volatiles within the sample surface had been trapped by the layer of SLS45.

The remaining calcium-based or magnesium-based layer worked as an effective coating, inhibiting the reaction process by blocking the exchange of solid and gas fuel with an oxidiser [52]. Moreover, the residues are non-combustible materials with low thermal conductivity, and so supplied additional physical protection.

The change in the wetted area was detected by the image processing, shown in Fig. 10. It can be seen that the water droplet had a larger wetting area than the other droplets in this study. It was also found that after the maximum spreading, there was rapid reduction of the water droplet's wetted area. The water droplet clustered into the centre and so the actual wetted area decreased dramatically, the typical image was shown in Fig. 10. The liquid layer, that formed, helped to prevent subsequent reactions, which acted as an additional mechanism of fire suppression. In contrast, the wetted area of the SLS20 and SDS20 droplets decreased more consistently with time which was due to the local boiling of the sub-droplets. The bubbling phenomenon along with the solid layer of SLS20/SDS20 droplets helped prevent the subsequent

combustion reactions effectively. The large layer continuously formed by the SLS45 droplet, with higher effectiveness at preventing the exchange of oxygen, due to the shell with high concentrations of solid content. The results of distilled water suggest that the evaporation had completed within 500 ms.

3.2. Schlieren imaging

Schlieren imaging was used to visualise the evolution of the single droplet impacting with a burning surface because it can be used to determine the change in density of the gas-phase product. In this work, a side view, high-speed Schlieren imaging system was arranged to obtain details which could not be visualised by direct imaging, such as the evaporation, vapor escape and phase change.

From Fig. 11, it can be seen that the intensive evaporation began 15 ms after the droplet impacted. Sub-droplets were observed to be ejected from the surface during the water droplet test. The vaporisation of droplets tended to be more stable with solid content concentration. The violent break-up of the droplet contributed to the escape of the vapor film which was between the parent droplet and the hot surface [53]. The $Ca(OH)_2$ and $Mg(OH)_2$ slurry acted as a shell to stabilise the violent vapor ejected from the parent droplet. The intense vaporisation can be observed in Fig. 11 (100 ms). The receding phenomenon caused the vaporisation of water droplet to occur at the centre of the burning surface, while SLS20 and SDS20 droplets tended to evaporate more consistently across the whole surface, similar to the observations in the direct imaging, in Fig. 8.

The SLS45 droplet performed differently from the others; it was observed that the droplet did not vaporise. Instead, the vapor occasionally escaped from the parent droplet, shown in Fig. 11 (red circle). High concentrations of $Ca(OH)_2$ solute formed a thick layer which suppressed the violent vapor because the inner pressure was not high enough to break free from the shell. The thick shell also acted as a sealant, blocking the oxidiser from the fuels which stopped the subsequent combustion reaction.

It is worth noting that weak evaporation of SLS20 and SDS20 droplets was observed after 600 ms which was not observed in the direct images. In comparison the water droplet completely evaporated before 600 ms elapsed. The weak evaporation occurring after 600 ms was likely attributed to the water generated by the carbonation process during combustion, taking into consideration the difference between the water contents of the droplets of distilled water and SLS20/SDS20 slurry [54]. A high concentration of carbon dioxide was generated from the combustion process and accelerated the carbonation reaction, generating water continuously. This delayed the surface temperature increasing after the initial extinguishing. The detailed results of surface temperature and the chemical components is presented in the next section.

3.3. Surface temperature

3.3.1. Single droplet

Thermal images supplied further information about the effectiveness of temperature inhibition by different liquid droplets, shown in Fig. 12. The temperature was averaged according to its maximum spreading area (shown in Fig. 3) to obtain comparative results. The surface temperature before the impacting was stable at approximately 525 °C for all cases. When the droplet impacted, the surface temperature dropped significantly which was attributed to cooling from the cold liquids. The evaporation occurred after a short delay (15 ms as shown in Fig. 11). Water evaporation is an effectively endothermic process [55], thus the surface temperature was reduced and remained stable at a low value. The surface temperature increased again after the water content had evaporated completely.

It can be seen from Fig. 12 that the rates of increase in temperature were different for each of the droplets when the intense evaporation ended. The surface temperature increase after the water droplet impact
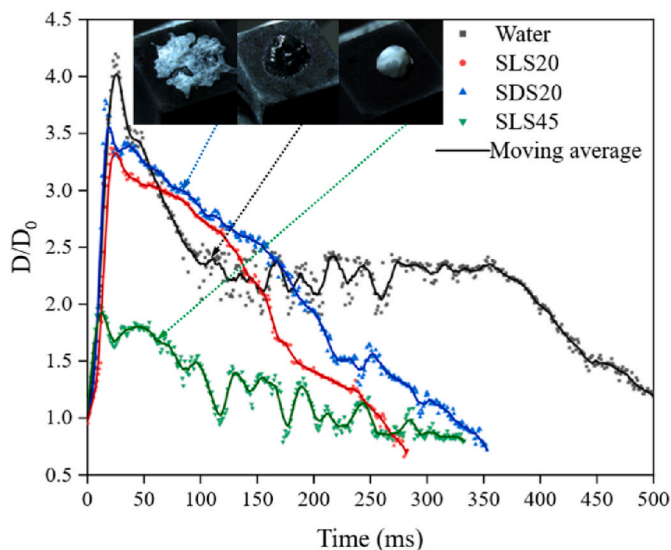

Fig. 10. The spread factor evolution of different droplets impacting with a burning surface.
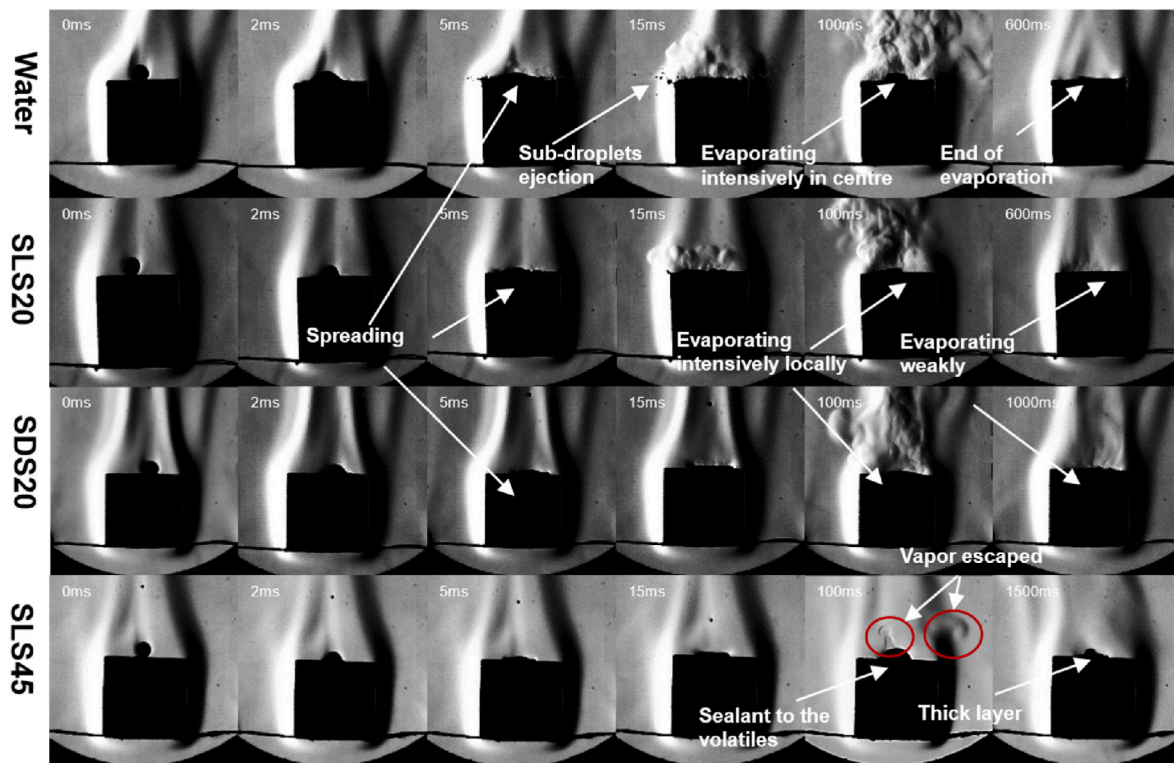
Fig. 11. Side view Schlieren images showing the process of the droplets impacting on a burning surface.
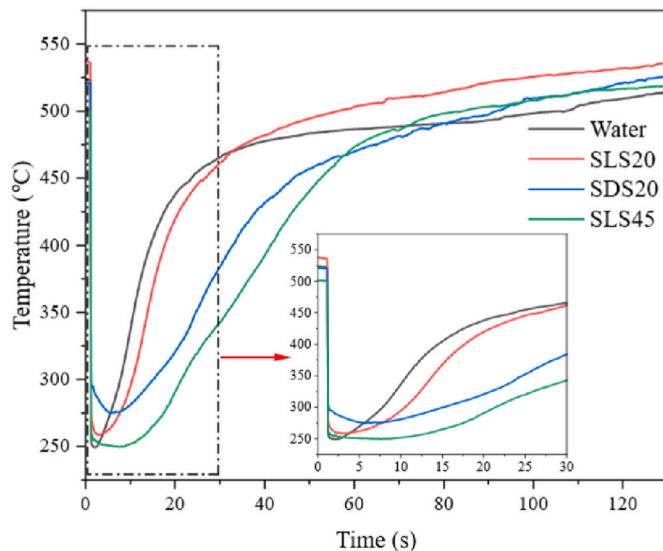

Fig. 12. The time evolution of averaged surface temperature for different component droplet impacts.

was the earliest and most rapid. The increase in surface temperature after the initial cooling was similar for the SLS20 droplet but had a noticeable delay compared to the water droplet. For SDS20 and SLS45, the increase was slower, and the temperature remained low for a relatively long period before it increased rapidly. Laoutid et al. reported that the heat release rate (HRR) was significantly reduced when the $Ca(OH)_2$ or $Mg(OH)_2$ fillers applied [25]. The formation of $CaCO_3$ as a combustion residue was the main reaction that inhibited the fire. The cohesive mineral residue hindered the combustion reaction by blocking the heat transfer and exchange of both gas-phase and solid-phase fuels and oxidisers. This was most apparent for the SLS45 droplet due to the high

solid content in the slurry. This work also found that the newly generated water (shown in Fig. 11) from the carbonation process delayed the temperature re-increase.

The InGaAs camera was used to monitor the evolution of the cooled area with a fixed threshold ($T < 300°C$). Fig. 13(a) shows the normalised cooled area size of the surface impacted by different droplets; the calculation was based on Eq. (3), Section 2.3. It is found that the cooled area ($T < 300°C$) of various droplets shrank at different rates. The cooled area of the water droplet decreased the fastest because the main temperature inhibition mechanism of pure water is evaporation which was insufficaint to prevent reignition. This is the reason that water extinguishers cannot effectively prevent the re-ignition of the biomass fuel [8]. Although SLS20 and SDS20 droplets have similar solid content quantities, the shrinking rate of the cooled area was different. Fig. 3 (b) shows the time when the cooled area shrank to 50% of the maximum area of the wetted region. The results were averaged from multiple tests and the standard deviations were shown as error bars. It can be seen from Fig. 13(b) that the surface impacted by the SDS20 droplet was at a low temperature for longer. This can also be seen in Fig. 12, where the surface temperature increased slower after the SDS20 droplet impact. This can be explained by the endothermic decomposition of magnesium hydroxide which occurs rapidly at a lower temperature ($T > 325°C$) [56] than calcium hydroxide ($T > 500°C$) [15,57]. Therefore, the endothermic reaction occurred sooner and at a lower temperature which makes SDS20 superior as a temperature suppressor. It is found in Fig. 13 (b) that the cooled area produced by the impacted of SLS45 droplets decreased the slowest. This can be explained by the cohesive mineral residue forming as a protective coating, which prevented the exchange of both heat and oxygen.

3.3.2. Different volumes

The surface temperature after impact with different volumes (Fig. 14 (a): single droplet, (b): 0.5 ml, (c): 1 ml, (d): 2 ml, (e): 3 ml, (f): 5 ml) of liquids was investigated in order to further compare the temperature inhibition performance of the different liquids. Generally, the ability of
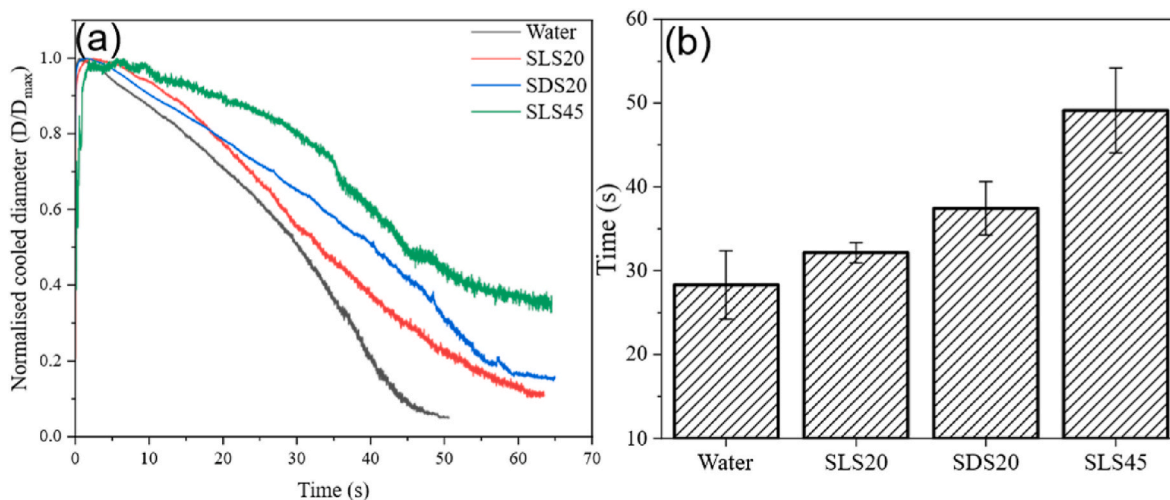
Fig. 13. (a) Normalised cooled area size ($T < 300°C$) of different component droplets and (b) the time when the cooled area shrank to 50% maximum wetted region and the standard deviation of multiple tests.
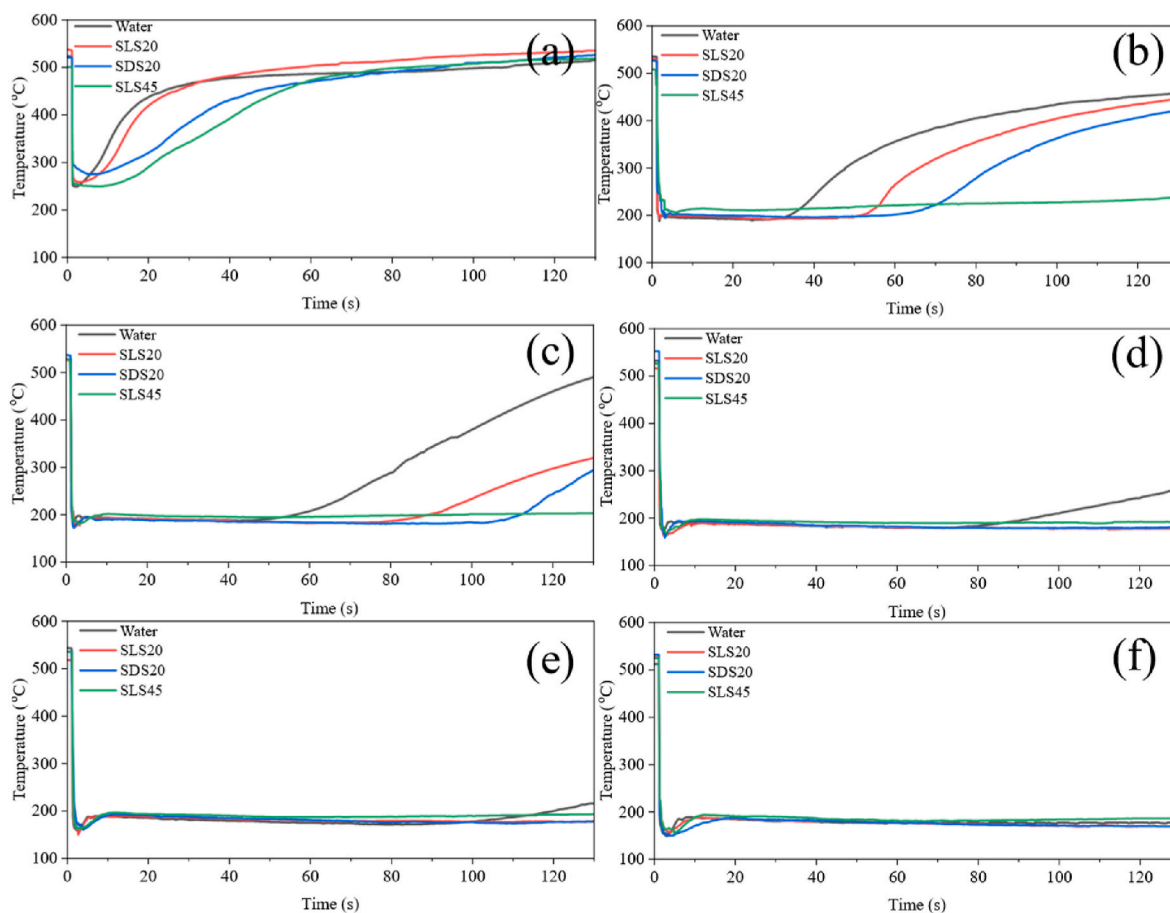

Fig. 14. The time evolution of the charcoal surface temperature impacted by various volumes of different liquids: single droplet (a), 0.5 ml (b), 1 ml (c), 2 ml (d), 3 ml (e), and 5 ml (f).

fire suppression was significantly different between the various liquids. Similar to the single droplet (Fig. 14 (a)), the delay before the temperature started to increase and the rates of the temperature re-increasing were different. They followed the same trend that SLS45 was the slowest, followed by the SDS20 and SLS20, while the post-evaporation temperature increase occurred earliest in the water tests. 0.5 ml SLS45 (Fig. 14 (b)) prevented a temperature re-increase within the test

duration (130 s). Comparatively, 2 ml of SLS20 and SDS20 was needed (Fig. 14 (d)) to achieve the same effect and distilled water required 5 ml (Fig. 14 (f)). Distilled water was used as the control group, and provided a representative time taken for the moisture to be completely removed. This was based on the assumpion that the temperature would only re-increase after the endothermic evaporation of the water content had ended. The temperature suppression effect after this point was the

contribution of additional mechanisms which have been demonstrated in the previous sections, such as the stable solid layers that impeded the combustion reactions, newly generated water, and the potential endothermic reactions.

Both calcium and magnesium hydroxide slurries performed better than the distilled water in terms of temperature inhibition. In addition, the high concentration of solid content was shown to be more effective due to it cutting off the reaction directly. The results also suggested that the adding of magnesium hydroxide could increase the effectiveness of fire suppression which was enabled by the decomposition at lower temperature.

4. Discussions

4.1. TGA analysis

$Ca(OH)_2$ and $Mg(OH)_2$ are unstable at high temperature [57]. It has been reported in the literature that the reaction of the calcium/magnesium hydroxide dehydration [58] could help with fire suppression [19,25]. Fig. 15 shows the results of the TGA experiments. This indicates the decomposition reactions of slaked samples under non-combustion circumstances. Considering the chemical components of SLS20 and SLS 45 were same, the TGA curves of these two samples were identical. The results show that there were three weight loss steps in SDS20 sample and two steps for SLS20 & SLS45. The first weight loss in SDS20 related to the dehydration of $Mg(OH)_2$ occurred 350 °C after the initial water loss [59]. The second weight loss was related to the dehydration of Ca(OH)2 occurred from the temperature of 430 °C above which was same in the SLS20 & SLS45 curve. The dehydration reactions are shown in Eqs. (6) and (7). These were slightly different to the tests from Koshiba Y. et al. [60] and Liang W. et al. [61] which resulted from the different particle size. The significant chemical reaction of dehydration occurred from the temperature above 512 °C according to the $CaO/Ca(OH)_2$ equilibrium [62].

Dehydration reactions:

$$Ca(OH)_2 \rightarrow CaO + H_2O \tag{6}$$

$$Mg(OH)_2 \rightarrow MgO + H_2O \tag{7}$$

The lime and dolime samples were produced from the calcination process, a small amount of carbonate was remained deliberately from an operational point of view [63]. The second weight loss step in SLS20 & SLS45 (third in SDS20) was identified as the decarbonation process of $CaCO_3$, shown in Eq. (8). This was found to occurred when the temperature was higher than 600 °C which is good agreement with the measurements conducted by Koshiba Y. et al. [60]. The decarbonation reaction of $MgCO_3$ (shown in Eq. (9)) starts at 450 °C [61]. Generating oxides (dehydration and decarbonation) is a typical endothermic
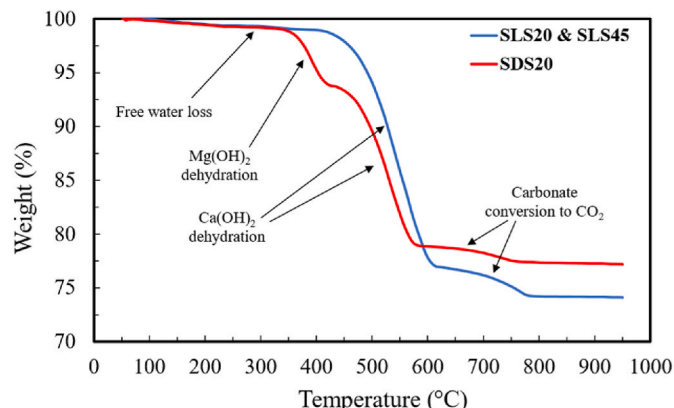

Fig. 15. TGA test of the pre-dried samples of SLS20 & SLS45 and SDS20.

reaction, thus the lower reaction temperatures of $Mg(OH)_2$ could help improve the effectiveness of fire inhibition at lower temperatures.

Decarbonation reactions:

$$CaCO_3 \rightarrow CaO + CO_2 \tag{8}$$
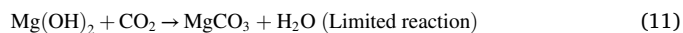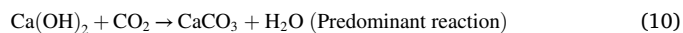
$$MgCO_3 \rightarrow MgO + CO_2 \tag{9}$$

4.2. XRD analysis

The fire inhibition performance of the calcium/magnesium hydroxide slurries was enhanced by the chemical changes. Therefore, it is of great interest to investigate the chemical components change at different times during the fire suppression process. The different test groups are indicated in Table .2. Although a single droplet cannot suppress the fire, investigation into the chemical change can help understand the anticipated mechanisms of fire inhibition in future studies.

Fig. 16 shows the X-ray diffraction (XRD) results of SLS20 (a), SDS20 (b) and SLS45 (c) samples heated at different times on the charcoal surface. The results demonstrated that the samples primarily contained calcium hydroxide and magnesium hydroxide (black line). The carbonation process occurred during the temperature re-increasing process which can be seen in Fig. 16 by the decrease in hydroxide along with increase in carbonate (red line). The carbonation reactions are shown in Eq. (10). and Eq. (11). CO_2 reacts readily with $Ca(OH)_2$, particularly in the presence of moisture, while the $Mg(OH)_2$ only has limited reaction with CO_2.

Carbonation reactions:

$$Ca(OH)_2 + CO_2 \rightarrow CaCO_3 + H_2O \text{ (Predominant reaction)} \tag{10}$$

$$Mg(OH)_2 + CO_2 \rightarrow MgCO_3 + H_2O \text{ (Limited reaction)} \tag{11}$$

The XRD results of 5 min heating duration show that the primary reaction of $Ca(OH)_2$ under the combustion circumstance was the carbonation reaction, the high concentration of CO_2 and the presence of moisture accelerated this process. It can be seen in Fig. 16 (blue lines) that most of the hydroxides decomposed completely before 5 min and the predominant product was $CaCO_3$ of the three testing samples. this supports the assumptions made in previous sections that the product of calcium carbonate helped prevent the subsequent combustion process. The observed water evaporation after 600 ms (Fig. 11) was the water generated from the carbonation. Although the carbonation process is an exothermic reaction, the heat can be effectively realised into the air by natural convection. In addition, the solid layer of $CaCO_3$ acted to insulate the surface from the air, inhibiting the combustion directly.

The surface temperature (Figs. 12 and 14) was not high enough to the $CaCO_3$ decomposition process, the identified CaO was produced from the dehydration reaction which is shown in Eq. (6). Combining with the conclusion of TGA in Fig. 15, it can be concluded two competing reactions, dehydration and carbonation, occurred simultaneously during this period with $CaCO_3$ and CaO ($MgCO_3$ and MgO) as residual precipitates on the surface. The surface temperature after 5 min of impacting was higher than the decomposition temperature of $MgCO_3$, therefore, the presence of MgO was also contributed to the decarbonation reaction. The limited $MgCO_3$ identified after 5 min indicates the primary product of magnesium compounds was MgO. The addition of $Mg(OH)_2$ could provide positive effects on the fire inhibition because of the endothermic reaction of oxides generation. The low decomposition temperature of $Mg(OH)_2$ could increase the effectiveness of the slurry at a lower temperature.

4.3. Conceptual model

Fig. 17 shows a summary of the temperature inhibition mechanisms of a droplet after impacting with a biomass fuel surface. Stage I shows the main evolution of a water droplet which has been reported in the
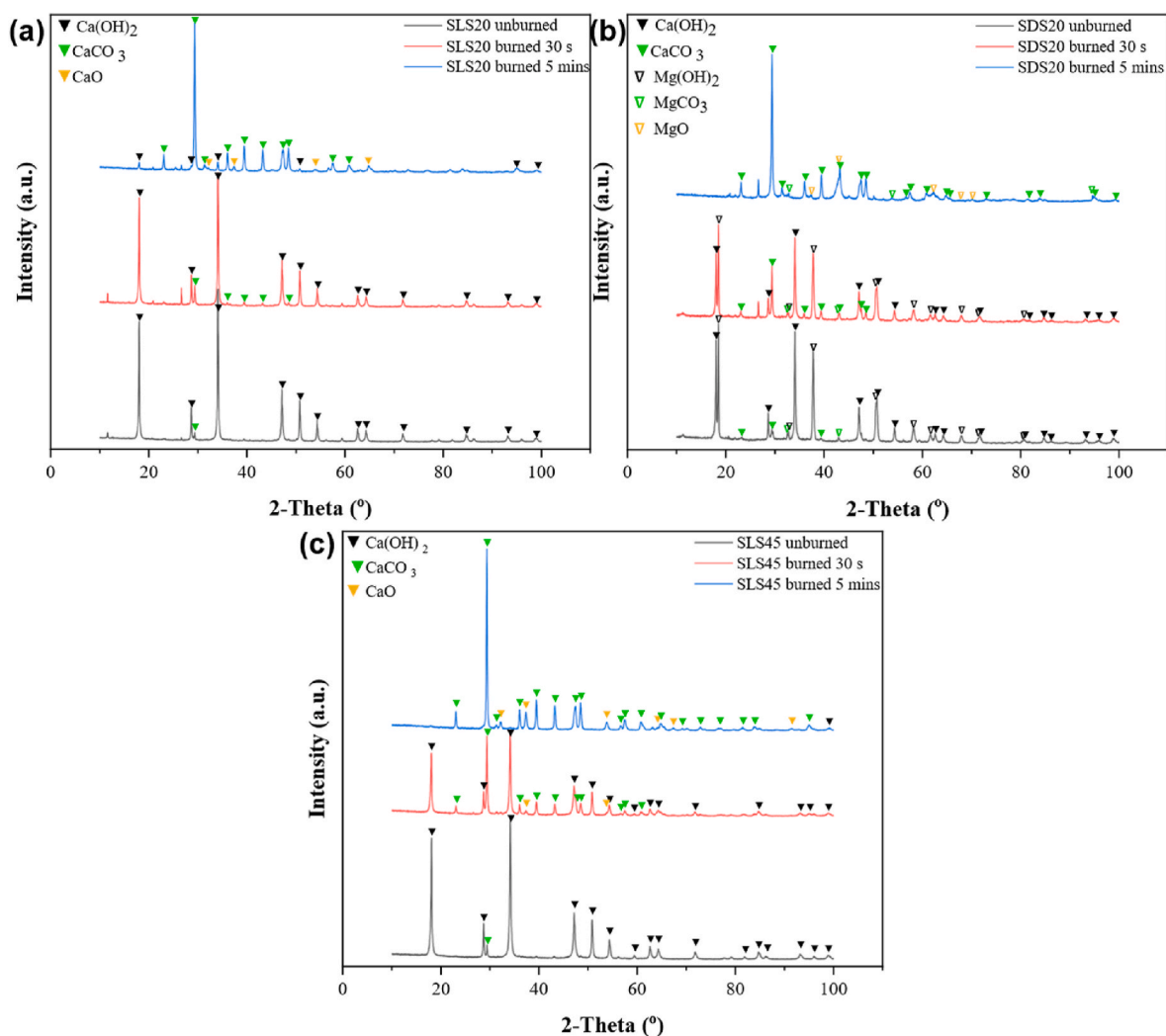
Fig. 16. XRD results of the remaining layers of various component single droplet impacted on the charcoal surface under different burning time: (a), SLS20 (b) SDS20 and (c) SLS45.

literature [31]. In detail, the distilled water suppressed the fire by cooling the fuel directly and the endothermic process of evaporation. Moreover, the observations in this work suggest that the receding droplet acted as a sealant that blocked the exchange of fuel and oxygen.

In addition to the distilled water droplet, $Ca(OH)_2$ and $Mg(OH)_2$ slurries have additional mechanisms that prevent the temperature re-increase of the biomass fuels, and significantly decrease the risk of the re-ignition, shown in Stage II and III in Fig. 17. According to the quantitative results and the visualisations in this work, it is found that the generated carbonate layer is the main mechanism that inhibits the solid fuel temperature increase. The carbonation occurred when the water evaporation had completed (>5s), shown in Fig. 16 (Stage II). The newly generated carbonates acted as a solid layer that protected the solid fuel surface from contact with external oxygen, preventing the subsequent combustion reactions. Additionally, the gas-phase fuel generated from the biomass pyrolysis could not escape from the layer of carbonates, hindering the combustion reaction. The continuous water generated from the carbonation and the subsequent evaporation (shown in Fig. 11) flattened the rate of temperature re-increasing. Although the generation of $CaCO_3$ is an exothermic reaction, it is insignificant compared with the combustion inhibition. Besides, the heat can easily release into the air, through the process of natural convection. Fig. 12 provides evidence in support of this proposition. Hamdani-Devarennes et al. [23] and Laoutid [25] also demonstrated that the thermal stable $CaCO_3$ layer helped the

fire-retardant performance with the exterior heat source or combustion. In our work, we have demonstrated that it has significant temperature suppression ability on the interior of a burning biomass fuel.

The TGA results show that dehydration occurred when the surface temperature has re-increased above 450 °C ($Ca(OH)_2$) and 350 °C (Mg $(OH)_2$). Although the oxides were not the predominant products, the presence of CaO and MgO suggested that the endothermic reactions help improve the fire inhibition ability. The carbonation and dehydration (Stage II) were competing reactions after the surface temperature re-increased (~60 s). The stable residues were produced by these reactions synchronously. The main product of magnesium compounds in the Stage II was MgO (shown in Fig. 16 (b)). The addition of $Mg(OH)_2$ could provide positive effects on the fire inhibition because its lower decomposition temperatures.

The thick carbonate layers also provide addition fire inhibition in the case of re-ignition under sufficient heat (stage III). $CaCO_3$ tends to decompose into CaO and CO_2 [64] and absorb a considerable amount of heat when the temperature is higher than 600 °C, shown in Eqs. (8) and (9). The exothermic reaction combined with the inhibition of combustion provides an effective protection in the case of fire.

5. Conclusions

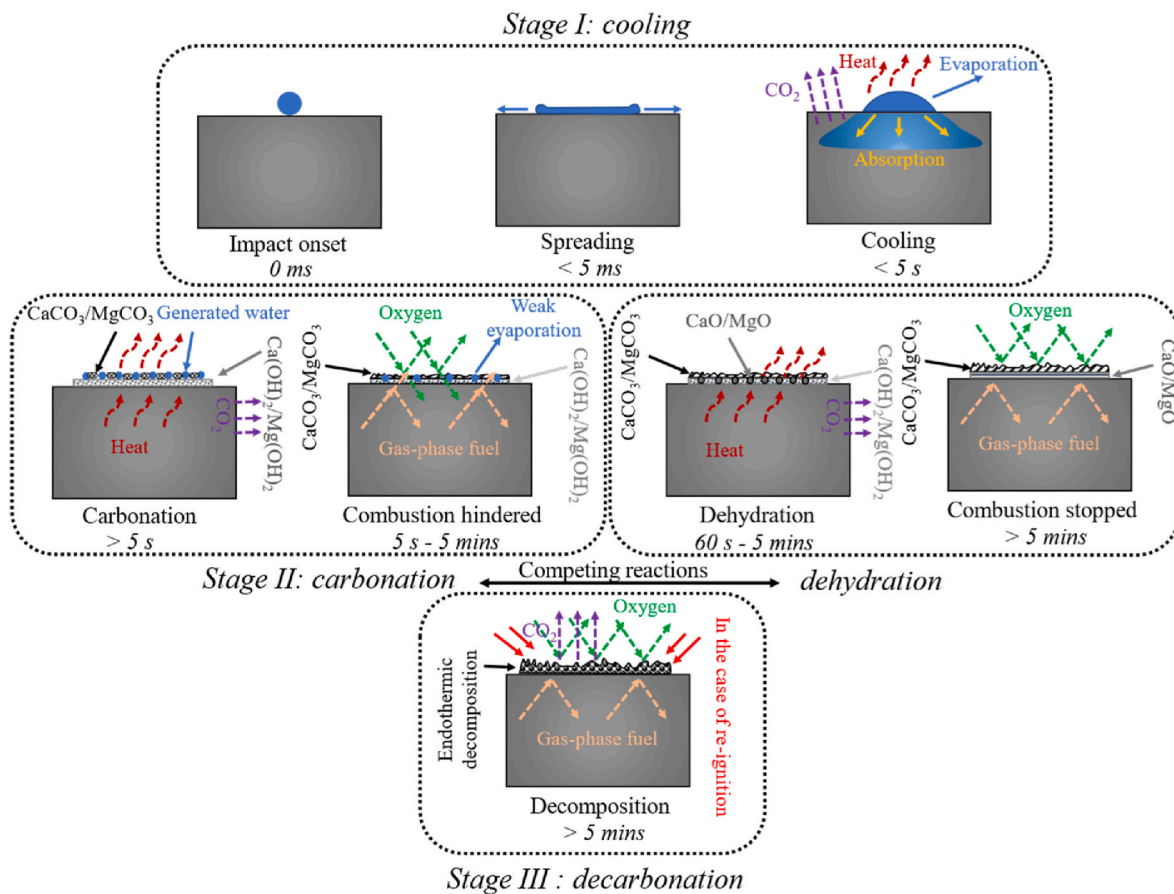The effectiveness of fire inhibition on a charcoal sample using

Fig. 17. Conceptual model of the fire inhibition mechanisms of the liquids: Stage I, for all types of liquids; Stage II, for SLS20/SDS20/SLS45 impacted on a burning surface. Stage III, in the case of the re-ignition of fire. The carbonation and dehydration (Stage II) were competing reactions after the temperature re-increasing process ended.

different types of slurries and distilled water was investigated rigorously. Charcoal was chosen as the fuel sample to best represent the characteristics of biomass fuel and the combustion reactions of coal. Three Stages: cooling, carbonation & dehydration and decarbonation were identified in the work. LWIR and SWIR thermal cameras were used to quantitatively measure the surface temperature and the cooled area size after post processing. The high-speed macro and Schlieren imaging were used for visualising the spreading and possible phase change. The results showed that SLS20, SDS20 and SLS45 slurries have better fire inhibition effectiveness when compared to the distilled water. In addition, either the mixture of $Mg(OH)_2$ (SDS20) and the increased content of $Ca(OH)_2$ (SLS45) could further improve the fire inhibition effectiveness. A conceptual model was built to demonstrate the mechanisms at different stages.

The specific conclusions gained from this research are:

1. Three stages were identified: water cooling, carbonation & dehydration and decarbonation.
2. The ability of spreading has been tested on both cold and burning surfaces, the results of which suggested that the water droplet had the highest spread factor, but intense receding phenomenon was found on the burning surface. On the other hand, the high solid content slurries had better adhesion capacity which intended to evaporate locally.
3. The stable solid layer of carbonates was considered as the main mechanism of temperature inhibition because the exchange of the oxygen and fuel was impeded effectively. The dehydration process as a competing reaction with carbonation, also contributed to improve the fire inhibition because the endothermic reaction.

Author statement

Yufeng Lai: Conceptualization, Methodology, Software, Formal analysis, Investigation, Data Curation, Writing - Original Draft. **Xuanqi Liu:** Methodology, Investigation, Data Curation, Writing - Review & Editing. **Callum Fisk:** Methodology, Writing - Review & Editing. **Matthew Davies:** Methodology, Writing - Review & Editing. **Yunbai Wang:** Methodology, Software, Visualisation, Writing - Review & Editing. **Jiansheng Yang:** Methodology, Software, Writing - Review & Editing. **Chris du Plessis:** Conceptualization, Resources, Writing - Review & Editing. **Liam Cotton:** Resources, Writing - Review & Editing. **Yang Zhang:** Resources, Writing - Review & Editing, Supervision. **Jon Willmott:** Conceptualization, Resources, Writing - Review & Editing, Supervision.

Data availability

Data will be made available on request.

References

[1] H. Gohar, et al., Investigating the characterisation, kinetic mechanism, and thermodynamic behaviour of coal-biomass blends in co-pyrolysis process, Process Saf. Environ. Protect. 163 (2022) 645–658.

[2] L. Liu, Y. Pang, D. Lv, K. Wang, Y. Wang, Thermal and Kinetic Analyzing of Pyrolysis and Combustion of Self-Heating Biomass Particles, vol. 151, Process Safety and Environmental Protection, 2021.

[3] Y. Zhang, Y. Zhang, Y. Li, X. Shi, S. Xia, Q. Guo, Determination and dynamic variations on correlation mechanism between key groups and thermal effect of coal spontaneous combustion, Fuel 310 (2022), 122454.

[4] D. Xue, et al., Carbon dioxide sealing-based inhibition of coal spontaneous combustion: a temperature-sensitive micro-encapsulated fire-retardant foamed gel, Fuel 266 (2020), 117036.

[5] Q. Zhou, B. Qin, Coal dust suppression based on water mediums: a review of technologies and influencing factors, Fuel 302 (2021), 121196.

[6] L. Ge, Y. Shao, Y. Wang, G. Zhang, Z. Zhang, L. Liu, Experimental research on inerting characteristics of carbon dioxide used for fire extinguishment in a large sealed space, Process Saf. Environ. Protect. 142 (2020) 174–190.

[7] A.O. Zhdanova, R.S. Volkov, I.S. Voytkov, K.Y. Osipov, G.v. Kuznetsov, Suppression of forest fuel thermolysis by water mist, Int. J. Heat Mass Tran. 126 (2018) 703–714.

[8] A. Liu, M.A. Delichatsios, Y.A. Levendis, On the trajectory and reach of fire-suppressant liquid nitrogen droplets released from a spray nozzle, Process Saf. Environ. Protect. 161 (2022) 273–284.

[9] Z. Xu, X. Guo, L. Yan, W. Kang, Fire-extinguishing performance and mechanism of aqueous film-forming foam in diesel pool fire, Case Stud. Therm. Eng. 17 (2020), 100578.

[10] B.Y. Lattimer, J. Trelles, Foam spread over a liquid pool, Fire Saf. J. 42 (2007) 249–264.

[11] S.A. Magrabi, B.Z. Dlugogorski, G.J. Jameson, A comparative study of drainage characteristics in AFFF and FFFP compressed-air fire-fighting foams, Fire Saf. J. 37 (2002) 21–52.

[12] A. Rotander, L.M.L. Toms, L. Aylward, M. Kay, J.F. Mueller, Elevated levels of PFOS and PFHxS in firefighters exposed to aqueous film forming foam (AFFF), Environ. Int. 82 (2015) 28–34.

[13] C. Yan, X. Pan, M. Hua, S. Li, X. Guo, C. Zhang, Study on the fire extinguishing efficiency and mechanism of composite superfine dry powder containing ferrocene, Fire Saf. J. 130 (2022), 103606.

[14] Y. Koshiba, Y. Takahashi, H. Ohtani, Flame suppression ability of metallocenes (nickelocene, cobaltcene, ferrocene, manganocene, and chromocene), Fire Saf. J. 51 (2012) 10–17.

[15] F. Carpentier, S. Bourbigot, M. le Bras, R. Delobel, M. Foulon, Charring of fire retarded ethylene vinyl acetate copolymer - magnesium hydroxide/zinc borate formulations, Polym. Degrad. Stabil. 69 (2000) 83–92.

[16] Z. Li, B. Qu, Flammability characterization and synergistic effects of expandable graphite with magnesium hydroxide in halogen-free flame-retardant EVA blends, Polym. Degrad. Stabil. 81 (2003) 401–408.

[17] K. Kuang, X. Huang, G. Liao, A comparison between superfine magnesium hydroxide powders and commercial dry powders on fire suppression effectiveness, Process Saf. Environ. Protect. 86 (2008) 182–188.

[18] M.S. Cross, P.A. Cusack, P.R. Hornsby, Effects of tin additives on the flammability and smoke emission characteristics of halogen-free ethylene-vinyl acetate copolymer, Polym. Degrad. Stabil. 79 (2003) 309–318.

[19] F. Laoutid, M. Lorgouilloux, D. Lesueur, L. Bonnaud, P. Dubois, Calcium-based hydrated minerals: promising halogen-free flame retardant and fire resistant additives for polyethylene and ethylene vinyl acetate copolymers, Polym. Degrad. Stabil. 98 (2013) 1617–1625.

[20] P. Lv, Z. Liu, J. Zhao, L. Pang, Inerting effect of CaCO3 powder on flame spread of wood dust layer, J. Loss Prev. Process. Ind. 82 (2023), 105000.

[21] C. Fluegeman, T. Hilton, K.P. Moder, R. Stankovich, Development of detailed action plans in the event of a sodium hydride spill/fire, Process Saf. Prog. 24 (2005) 86–90.

[22] Y. Koshiba, T. Haga, H. Ohtani, Flame inhibition by calcium compounds: effects of calcium compounds on downward flame spread over solid cellulosic fuel, Fire Saf. J. 109 (2019), 102865.

[23] S. Hamdani-Devarennes, C. Longuet, R. Sonnier, F. Ganachaud, J.M. Lopez-Cuesta, Calcium and aluminum-based fillers as flame-retardant additives in silicone matrices. III. Investigations on fire reaction, Polym. Degrad. Stabil. 98 (2013) 2021–2032.

[24] Y.A. Criado, M. Alonso, J.C. Abanades, Kinetics of the CaO/Ca(OH) 2 hydration/dehydration reaction for thermochemical energy storage applications, Ind. Eng. Chem. Res. 53 (2014) 12594–12601.

[25] F. Laoutid, M. Lorgouilloux, L. Bonnaud, D. Lesueur, P. Dubois, Fire retardant behaviour of halogen-free calcium-based hydrated minerals, Polym. Degrad. Stabil. 136 (2017) 89–97.

[26] Z. Huang, et al., Inhibition characteristics of a novel PAM/SA-Ca(OH)2 composite inhibitor to control coal spontaneous combustion, Fuel 314 (2022), 122750.

[27] N. Gao, K. Chen, C. Quan, Development of CaO-based adsorbents loaded on charcoal for CO2 capture at high temperature, Fuel 260 (2020), 116411.

[28] M. Heidari, M. Tahmasebpoor, A. Antzaras, A.A. Lemonidou, CO2 capture and fluidity performance of CaO-based sorbents: effect of Zr, Al and Ce additives in tri-, bi- and mono-metallic configurations, Process Saf. Environ. Protect. 144 (2020) 349–365.

[29] P. César de Carvalho Pinto, G. Voga Pereira, L. Schiavo de Rezende, F.C.C. Moura, J. Cláudio Belchior, CO2 capture performance and mechanical properties of Ca (OH)2-based sorbent modified with MgO and (NH4)2HPO4 for Calcium Looping cycle, Fuel 256 (2019), 115924.

[30] A. Yoshida, R. Takasaki, K. Kashiwa, H. Naito, Y. Saso, Extinguishment of counterflow methane/air diffusion flame by polydisperse fine water droplets, Combust. Flame 160 (2013) 1357–1363.

[31] A. Albadi, Y. Zhang, Experimental study of water droplet impact on burning wood surfaces, Proc. Combust. Inst. 38 (2021) 4605–4613.

[32] Y. Lai, X. Wang, T.B.O. Rockett, J.R. Willmott, H. Zhou, Y. Zhang, The effect of preheating on fire propagation on inclined wood by multi-spectrum and schlieren visualisation, Fire Saf. J. 118 (2020), 103223.

[33] R. Payri, J. Gimeno, P. Martí-Aldaraví, C. Carvallo, Parametrical study of the dispersion of an alternative fire suppression agent through a real-size extinguisher system nozzle under realistic aircraft cargo cabin conditions, Process Saf. Environ. Protect. 141 (2020) 110–122.

[34] Y. Lai, X. Wang, T.B.O. Rockett, J.R. Willmott, Y. Zhang, Investigation into wind effects on fire spread on inclined wooden rods by multi-spectrum and schlieren imaging, Fire Saf. J. 127 (2022), 103513.

[35] Y. Lai, A. Albadi, X. Liu, M. Davies, M. Hobb, J.R. Willmott, Y. Zhang, Investigation of forced flow orientations on the burning behaviours of wooden rods using a synchronised multi-imaging system, Proc. Combust. Inst. 39 (2022).

[36] F.L. Browne, Theories of the Combustion of Wood and its Control, 1955.

[37] R.A. Bradstock, Effects of large fires on biodiversity in south-eastern Australia: disaster or template for diversity, Int. J. Wildland Fire 17 (2008) (2008) 809–822.

[38] A. Vanaparti, Experimental Study of Radiative Properties of Charcoal Combustion in Grills, 2016.

[39] J.H. Lin, J.C. Jhang, T.A. Lin, S.Y. Huang, Y.S. Chen, C.W. Lou, Manufacturing techniques, mechanical properties, far infrared emissivity, and electromagnetic shielding effectiveness of stainless steel/polyester/bamboo charcoal knits, Fibers Polym. 18 (2017) 597–604.

[40] L.A. Dombrovsky, S. Dembele, J.X. Wen, A simplified model for the shielding of fire thermal radiation by water mists, Int. J. Heat Mass Tran. 96 (2016) 199–209.

[41] A. Chengara, A.D. Nikolov, D.T. Wasan, Spreading of a water drop triggered by the surface tension gradient created by the localized addition of a surfactant, Ind. Eng. Chem. Res. 46 (2007) 2987–2995.

[42] D.D. Evans, H.W. Emmons, Combustion of wood charcoal, Fire Saf. J. 1 (1977) 57–66.

[43] K. Prabhakar, R.C. Maheshwari, O.P. Vimal, Pyrolysis of coconut shell and its potential as fuel, Agric. Waste 17 (4) (1986) 313–317.

[44] J.D. Bustos-Vanegas, M.A. Martins, A.G. Freitas, J. Mellmann, Experimental characterization of self-heating behavior of charcoal from eucalyptus wood, Fuel 244 (2019) 136.

[45] M.J. Hobbs, A. Barr, S. Woolford, D. Farrimond, S.D. Clarke, A. Tyas, J.R. Willmott, High-speed infrared radiation thermometer for the investigation of early stage explosive development and fireball expansion, Sensors 22 (2022) 6143.

[46] Y. Sawada, Y. Ito, Thermal decomposition of calcium hydroxide deposited on the substrate, Thermochim. Acta 232 (1994) 47–54.

[47] R. Rioboo, M. Marengo, C. Tropea, Time evolution of liquid drop impact onto solid, dry surfaces, Exp. Fluid 33 (2002) 112–124.

[48] P.M. Bhagat, Wood charcoal combustion and the effects of water application, Combust. Flame 37 (1980) 275–291.

[49] M. Olsson, G. Petersson, Benzene emitted from glowing charcoal, Sci. Total Environ. 303 (2003) 215–220.

[50] M.B. Tilghman, R.E. Mitchell, Coal and biomass char reactivities in gasification and combustion environments, Combust. Flame 162 (2015) 3220–3235.

[51] D. Drysdale, An Introduction to Fire Dynamics, John Wiley & Sons, 2011.

[52] J.H. Beh, M.K. Yew, M.C. Yew, L.H. Saw, Characterization and fire protection properties of rubberwood biomass ash formulated intumescent coatings for steel, J. Mater. Res. Technol. 14 (2021) 2096–2106.

[53] U. Sen, T. Roy, R. Ganguly, L.A. Angeloni, W.A. Schroeder, C.M. Megaridis, Explosive behavior during binary-droplet impact on superheated substrates, Int. J. Heat Mass Tran. 154 (2020), 119658.

[54] R.N. Rothon, Effects of Particulate Fillers on Flame Retardant Properties of Composites, second ed., 2003. Shrewsbury.

[55] C. Doursat, L. Lecoq, O. Laguerre, D. Flick, Droplet evaporation on a solid surface exposed to forced convection: experiments, simulation and dimensional analysis, Int. J. Heat Mass Tran. 113 (2017) 1234–1245.

[56] I. Shancita, N.G. Vaz, G.D. Fernandes, A.J.A. Aquino, D. Tunega, M.L. Pantoya, Regulating magnesium combustion using surface chemistry and heating rate, Combust. Flame 226 (2021) 419–429.

[57] B.Q. Xia, Z.H. Pan, J. Yan, C.Y. Zhao, Mesoscopic exploration on mass transfer in porous thermochemical heat storage materials, Int. J. Heat Mass Tran. 135 (2019) 52–61.

[58] S. Lin, Y. Wang, Y. Suzuki, High-temperature CaO hydration/ca(OH)2 decomposition over a multitude of cycles, Energy Fuel. 23 (2009) 2855–2861.

[59] D. Du, X. Shen, L. Feng, M. Hua, X. Pan, Efficiency characterization of fire extinguishing compound superfine powder containing Mg(OH)2, J. Loss Prev. Process. Ind. 57 (2019).

[60] Y. Koshiba, Y. Hirakawa, Fire-suppression Efficiency and Extinguishing Mechanisms of Calcium Acetate Using Heptane Cup-Burner Flames, Fire Mater, 2023.

[61] W. Liang, Y. Yin, L. Wang, L. Chen, H. Li, A new method of preparing anhydrous magnesium carbonate (MgCO3) under high pressure and its thermal property, J. Alloys Compd. 702 (2017).

[62] Y.A. Criado, M. Alonso, J.C. Abanades, Kinetics of the CaO/Ca(OH)2 hydration/dehydration reaction for thermochemical energy storage applications, Ind. Eng. Chem. Res. 53 (2014).

[63] C.A. du Plessis, H. Lambert, R.S. Gärtner, K. Ingram, W. Slabbert, J.J. Eksteen, Lime use in gold processing – a review, Miner. Eng. 174 (2021).

[64] Z.S. Li, F. Fang, X.Y. Tang, N.S. Cai, Effect of temperature on the carbonation reaction of CaO with CO 2, Energy Fuel. 26 (2012) 2473–2482.